Calculated cross sections and measured rate coefficients for electron-impact excitation of neutral and singly ionized nitrogen

R. M. Frost[a] and P. Awakowicz
Lehrstuhl für Technische Elektrophysik, Technische Universität München, Arcisstraße 21, 80333 München, Germany

H. P. Summers and N. R. Badnell
Department of Physics and Applied Physics, University of Strathclyde, Glasgow, G4 0NG, United Kingdom

(Received 5 January 1998; accepted for publication 12 June 1998)

R-matrix calculations for neutral (N I) and singly ionized nitrogen (N II) have been carried out in the energy region below 50 eV for N I and 180 eV for N II, respectively. The collision strengths were calculated for optical allowed and forbidden transitions as well as for exchange transitions involving energy levels with principal quantum numbers $n \leqslant 3$. In both atomic systems, spectroscopic measurements in the visible and vacuum-ultraviolet spectral range have been performed in order to investigate several rate coefficients in the theoretically uncertain near-threshold regions. For this purpose seven N I- and sixteen N II-rate coefficients were determined by means of a 7 mm diameter stationary cascade arc discharge operated at a current of 8 A and different pressures in the range from 1 to 30 hPa. The spectroscopic system for the vacuum-ultraviolet wavelength range was intensity calibrated by means of the continuum radiation of a normal pressure pure helium arc discharge and the calibrated line emission of a hollow cathode lamp. Plasma diagnostics yielded electron densities from 1.8 to 7.0×10^{13} cm^{-3}. By applying a collisional-radiative model the rate coefficients were obtained from absolute level densities. This collisional-radiative model also yielded the ground and metastable state number densities on the basis of calculated rate coefficients for optical allowed transitions. Variation of the arc pressure resulted in electron temperatures ranging from 4.5 to 8.4 eV. Over this range the calculated rate coefficients have been partly confirmed by experimental ones. © *1998 American Institute of Physics.* [S0021-8979(98)02718-2]

I. INTRODUCTION

A. General

In the last 15 years, low density plasmas have gained increasing importance in many different technical applications. Microwave, rf and dc plasma reactors are being used for plasma processing such as reactive ion etching or thin film deposition. These low density plasmas are comparable in many respects. For example, the kinetic temperature of the atoms and ions is always much lower than that of the electrons. So, the plasmas are generally far from local thermal equilibrium (LTE), a situation which complicates the analysis of the plasma state to a great extent. Depending on the individual energy levels and particular plasma conditions, however, a relatively simple model can be applied, namely, the balance between collisional excitation/ionization and spontaneous radiative decay, called coronal equilibrium. In this case, the knowledge of cross sections of electron-impact excitation and ionization is necessary for the different atomic systems. In the intermediate electron density region as reported here, redistribution amongst excited states by means of collisional processes as well as radiative transitions from upper to lower lying levels must be taken into account. This means that plasma modeling on the basis of collisional-radiative models is required which is often complicated by radiative transfer and diffusion processes. Due to the uncertainties of the pertinent rate coefficients, experimental investigation of such models and the included cross sections is highly desirable. The low ionization stages of nitrogen are interesting for several reasons. In low temperature rf discharges, nitrogen is used for technological applications like hard coatings or to improve the textured growth of diamond. In fusion Tokamak reactors, nitrogen is puffed into the divertor chamber to actively cool the energetic particles flowing down the scrape-off-layer. The present article deals mainly with R-matrix calculations and spectroscopic measurements to investigate the collisional-radiative models and the rate coefficients of atomic and ionized nitrogen. Thus, the collisional processes were based on cross sections for electron-impact excitation calculated by the R-matrix method. For the experimental investigations, a cascade arc was operated at low pressure and relatively low current in order to reduce the electron density to the range of interest. Variation of the electron temperature and density was achieved by using different pressures. In these low density arc plasmas, spectroscopic measurements were performed in the visible (vis) and the vacuum-ultraviolet (VUV) wavelength range.

B. Procedure

In Fig. 1 the schematic of the combined investigations, namely, the R-matrix calculations, the plasma diagnostics,

[a]Electronic mail: frost@tep.e-technik.tu-muenchen.de

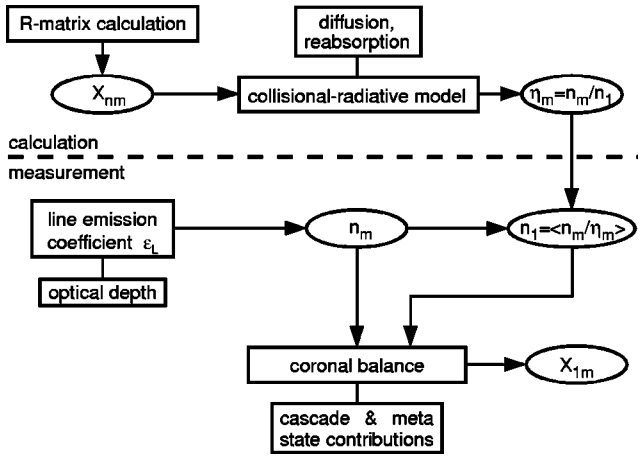

FIG. 1. Schematic drawing of the experimental determination of the rate coefficients.

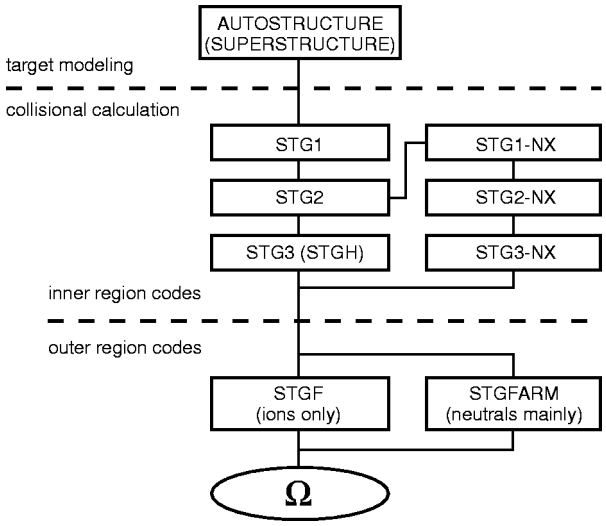

FIG. 2. Schematic drawing of the calculations done by the different codes.

and the determination of the rate coefficients via a collisional-radiative model is shown. In Sec. II, a brief description of the R-matrix calculations, which provided the cross sections of the different transitions caused by electron-impact, will be given. The rate coefficients were obtained by integrating the cross sections over a Maxwellian distribution of the free electrons. The calculated coefficients were inserted in a collisional-radiative model thus yielding population densities related to the ground state density. The *Atomic Data and Analysis Structure ADAS*[1] was used for this purpose (*ADAS* 208, see Sec. V). In Sec. III, the experimental setup and its absolute intensity calibration in the visible and VUV spectral range is presented. This was based on the helium continuum radiation of a normal-pressure cascade arc and calibrated line radiation of a hollow cathode. The plasma diagnostics, namely, the determination of the temperature of the heavy particles, of the electron density, and of the electron temperature, are pointed out in Sec. IV. The population densities of the ground and metastable states were obtained by dividing the measured absolute population densities of levels radiating by electric dipole transition to the ground state (see Sec. V) with the aforementioned calculated relative population densities. Levels exited by electric dipole collisional transitions are preferred because they are theoretically better known than nondipole or exchange transitions. Once the ground and metastable state densities are known, it is possible to obtain rate coefficients for electron-impact excitation from these ground levels to a multitude of excited levels, if the line emission resulting from spontaneous radiative decay of these excited levels is measurable. In Sec. VI, results of the calculated and measured rate coefficients will be discussed and compared.

II. R-MATRIX CALCULATIONS

The N I and N II target structures have been modelled by using *AUTOSTRUCTURE*,[2] a code developed from the older *SUPERSTRUCTURE*.[3] An additional option of *AUTOSTRUCTURE* is to calculate the radial functions in a Hartree potential and evaluate them by Slater-type orbitals resulting in one optimization parameter $\lambda_{nl}\sim 1$ for each orbital nl. By minimizing a suitable linear combination of the resulting energies E_{nl} by adjusting this parameter, an optimization process is engendered. In addition, it is possible to use nonphysical pseudo-orbitals in order to adjust the calculated level energies with respect to experimental ones.

The target modeling for neutral nitrogen included the $2s^22p^3$, $2s2p^4$, $2s^22p^23s$, $2s^22p^23p$, $2s^22p^23d$, $2s2p^33s$ and the $2p^5$ configurations. The latter two were treated as correlation configurations resulting in a 33 term close-coupling collision calculation. For the ion, we used the $2s^22p^2$, $2s2p^3$, $2s^22p3s$, $2s^22p3p$, $2s^22p3d$ and the $2p^4$ configurations. All resulting 23 terms were included in the close-coupling calculation. We found that the introduction of a small number of $(n=4)$ pseudo-orbitals did not increase the accuracy of our atomic structure (oscillator strengths and term energies) significantly and so we omitted them. This reduced the calculation time and made best use of the available computer resources.

The R-matrix close-coupling calculations for the collision strengths Ω were carried out using inner-region exchange[4] and nonexchange[5] and outer region (*STGFARM*[6] and *STGF*[7]) codes. The present setup of these codes enables smooth passage of data from step to step. Figure 2 gives an overview of the connection of the different codes. In the case of exchange transitions, good convergence may be obtained with partial wave expansions excluding high angular momenta L of the $(N+1)$-electron system. This is due to the fact that the collision strengths of these transitions are proportional to E^{-2} for $E\rightarrow\infty$, where E means the energy of the incident electron. In contrast, the collision strengths of the dipole and nondipole nonexchange transitions show an asymptotic behavior proportional to $\ln E$ and constant with E, respectively. Therefore, it is necessary for them to consider contributions obtained from very high L's. The codes for nonexchange transitions (NX codes) shown in Fig. 2 which do not calculate exchange transitions are numerically more stable at high L values. These codes were used to calculate the high-L contributions to Ω for the dipole and non-

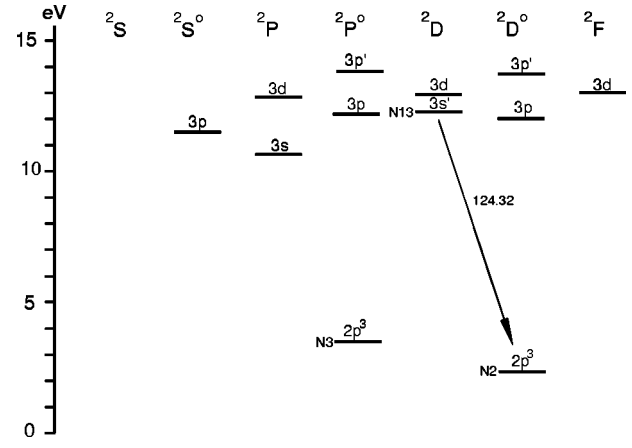

FIG. 3. Grotrian diagram of the N I doublet system. (Only transitions measured in this investigation are shown.)

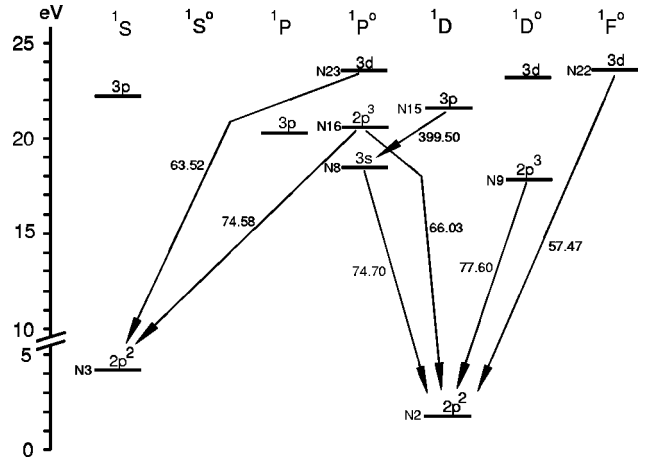

FIG. 5. Grotrian diagram of the N II singlet system. (Only transitions measured in this investigation are shown.)

dipole nonexchange transitions until good convergence had been reached.

The collision strength $\Omega_{m,n}$ for an electron-impact induced transition between the initial state m and the final state n is related to the corresponding cross section $\sigma_{m,n}$ by

$$\Omega_{m,n}(E)=\Omega_{n,m}(E)=g_m\frac{E}{I_H}\frac{\sigma_{m,n}(E)}{\pi a_0^2}. \tag{2.1}$$

Herein, g_m is the statistical weight of the level m, a_0 the Bohr radius and I_H the Rydberg energy. Maxwellian averaging of the cross section then yields the rate coefficient for the electron-impact excitation process

$$X_{m,n}(T_e)=\int_{\Delta E_{m,n}}^{\infty}\sigma_{m,n}(E)v(E)f_m(E,T_e)dE \tag{2.2}$$

with the electron temperature T_e, the threshold energy $\Delta E_{m,n}$, the electron velocity v and the Maxwellian distribution function f_m. Finally, the relation between the rate coefficients for excitation and de-excitation is given by

$$X_{n,m}=X_{m,n}\frac{g_m}{g_n}\exp\left\{-\frac{E_m-E_n}{kT_e}\right\}. \tag{2.3}$$

To avoid inconvenient usage of the strongly temperature dependent rate coefficient, one often uses the effective collision strength or rate parameter $\gamma_{m,n}$ which is related to the rate coefficient as follows:

$$X_{m,n}(T_e)=2\sqrt{\pi}\alpha c a_0^2\sqrt{\frac{I_H}{kT_e}}\frac{\gamma_{m,n}(T_e)}{g_m}\exp\left\{-\frac{\Delta E_{m,n}}{kT_e}\right\}, \tag{2.4}$$

where α is the fine structure constant.

The lowest 21 terms are shown in Figs. 3 and 4 for the neutral atom and all terms (except $^5S^o$) in Figs. 5 and 6 for the ion. In addition, they are listed in Tables I and II along with their statistical weights and term energies. These tables also assign arbitrary term numbers to the terms which are necessary for the designation of the calculated rate coefficients of which a collection is listed as rate parameters in Tables III and IV.

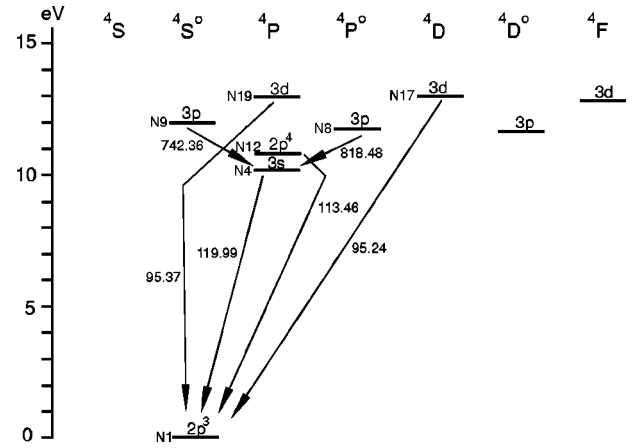

FIG. 4. Grotrian diagram of the N I quartet system. (Only transitions measured in this investigation are shown.)

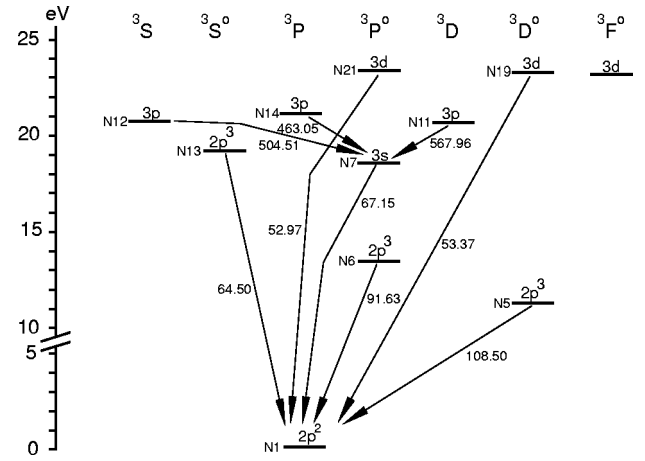

FIG. 6. Grotrian diagram of the N II triplet system. (Only transitions measured in this investigation are shown.)

TABLE I. Energy levels of the nitrogen atom: the configurations and term symbols are listed together with the corresponding statistical weights g_m and energies E_m.[a] (The spectroscopic notation is corresponding to Moore.[b])

No.	Configuration	Term	g_m	$E_m(\mathrm{cm}^{-1})$
1	$2s^2 2p^3$	$^4S^o$	4	0.
2	$2s^2 2p^3$	$^2D^o$	10	19227.
3	$2s^2 2p^3$	$^2P^o$	6	28839.
4	$2s^2 2p^2(^3P)3s$	^4P	12	83335.
5	$2s^2 2p^2(^3P)3s$	^2P	6	86192.
6	$2s^2 2p^2(^3P)3p$	$^2S^o$	2	93581.
7	$2s^2 2p^2(^3P)3p$	$^4D^o$	20	94837.
8	$2s^2 2p^2(^3P)3p$	$^4P^o$	12	95509.
9	$2s^2 2p^2(^3P)3p$	$^4S^o$	4	96750.
10	$2s^2 2p^2(^3P)3p$	$^2D^o$	10	96833.
11	$2s^2 2p^2(^3P)3p$	$^2P^o$	6	97793.
12	$2s2p^4$	^4P	12	88132.
13	$2s^2 2p^2(^1D)3s'$	^2D	10	99663.
14	$2s^2 2p^2(^3P)3d$	^2P	6	104628.
15	$2s^2 2p^2(^3P)3d$	^4F	28	104719.
16	$2s^2 2p^2(^3P)3d$	^2F	14	104850.
17	$2s^2 2p^2(^3P)3d$	^4D	20	105007.
18	$2s^2 2p^2(^3P)3d$	^2D	10	105134.
19	$2s^2 2p^2(^3P)3d$	^4P	12	104856.
20	$2s^2 2p^2(^1D)3p'$	$^2D^o$	10	110535.
21	$2s^2 2p^2(^1D)3p'$	$^2P^o$	6	112311.

[a]See Ref. 20.
[b]See Ref. 38.

TABLE II. Energy levels of the singly charged nitrogen ion: the configurations and term symbols are listed together with the corresponding statistical weights g_m and energies E_m.[a] (The spectroscopic notation is corresponding to Moore.[b])

No.	Configuration	Term	g_m	$E_m(\mathrm{cm}^{-1})$
1	$2s^2 2p^2$	^3P	9	89.
2	$2s^2 2p^2$	^1D	5	15194.
3	$2s^2 2p^2$	^1S	1	32522.
4	$2s2p^3$	$^5S^o$	5	46579.
5	$2s2p^3$	$^3D^o$	15	91931.
6	$2s2p^3$	$^3P^o$	9	108866.
7	$2s^2 2p(^2P)3s$	$^3P^o$	9	148559.
8	$2s^2 2p(^2P)3s$	$^1P^o$	3	148734.
9	$2s2p^3$	$^1D^o$	5	143742.
10	$2s^2 2p(^2P)3p$	^1P	3	164114.
11	$2s^2 2p(^2P)3p$	^3D	15	166117.
12	$2s^2 2p(^2P)3p$	^3S	3	168394.
13	$2s2p^3$	$^3S^o$	3	154656.
14	$2s^2 2p(^2P)3p$	^3P	9	170124.
15	$2s^2 2p(^2P)3p$	^1D	5	173692.
16	$2s2p^3$	$^1P^o$	3	166271.
17	$2s^2 2p(^2P)3p$	^1S	1	177743.
18	$2s^2 2p(^2P)3d$	$^3F^o$	21	186040.
19	$2s^2 2p(^2P)3d$	$^3D^o$	15	186927.
20	$2s^2 2p(^2P)3d$	$^1D^o$	5	186544.
21	$2s^2 2p(^2P)3d$	$^3P^o$	9	188328.
22	$2s^2 2p(^2P)3d$	$^1F^o$	7	188777.
23	$2s^2 2p(^2P)3d$	$^1P^o$	3	189565.

[a]See Ref. 21.
[b]See Ref. 38.

III. EXPERIMENTAL SETUP AND ABSOLUTE CALIBRATION OF THE SYSTEM RESPONSE

A. Experimental setup

To investigate the rate coefficients of neutral and singly ionized nitrogen, a stationary low pressure plasma was generated in a Maecker-type cascaded arc chamber.[8] As shown in Fig. 7, the cascade itself consists of a stack of axially insulated, water-cooled copper plates with aligned center bores of 7 mm diameter forming the discharge channel. Silicon rubber rings between the plates are used as vacuum seals.

Two tungsten electrodes on the anode side, fed by separate ballast resistors, share the current load. The cathode was built as a V-shaped tungsten wire connected to two molybdenum rods at both ends. The rods are inserted in two electrical insulated brass tubes, which are water cooled. The cathode is electrical heated up to 3000 K because there are not enough positive ions transferring sufficient energy to heat the cathode properly. The base of all three electrodes is shielded by means of boron nitride plates.

For the following N I and N II measurements, the discharge was operated at 8 A current and at pressure values between 100 and 3000 Pa. The original arc design as described in Ref. 8 was substantially modified for operation at lower pressures. Thus the stack of cascade plates was isolated further from the ambient atmosphere by a vacuum-tight plexiglas cylinder. The buffer volume between this cylinder and the cascade was pumped by a turbomolecular pump, which considerably reduced the influx of atmospheric nitrogen and oxygen into the arc chamber through leaks of the many silicon rubber seals. Further changes concerned the construction of flanges, windows, electrodes, and the complete gas pumping system.

The plasma consisted mainly of helium with only a 0.2% admixture of nitrogen. The gas composition was adjusted by calibrated mass flow controllers. Figure 8 shows the VUV spectrum at a pressure of 800 Pa. For this scan, a very large amount of nitrogen has been added to show the lines clearly.

As shown in Fig. 9 the discharges were investigated simultaneously by two optical systems, observing end-on nearly the same central region of the plasma column from opposite directions. A 2-m monochromator for the visible region at the cathode side of the arc served for diagnostic purposes in the wavelength range 250–830 nm. This instrument has a spectral resolution of 15 pm in the first spectral order. The plasma intensities were recorded by a photomultiplier (N I/N II investigations: R928, calibration of the VUV system: 1P28a) behind the exit slit. For precise wavelength scans, photomultiplier and exit slit were moved together in the focal plane by a precision mechanical drive. For scans of narrow line profiles, a piezo driven shift unit was connected to the mechanical drive and the monochromator was operated in the minus fifth order resulting in a spectral resolution of 2.6 pm. The system response was calibrated by a tungsten strip lamp, which had itself been calibrated at the Physikalisch Technische Bundesanstalt Berlin.

From the other direction, the VUV system served for intensity measurements of the different plasmas. A platinum-coated spherical mirror focused the cross section of the plasma column on the entrance slit of a 1-m McPherson monochromator. The concave grating surface also consisted

TABLE III. Calculated effective collision strengths $\gamma_{m\to n}$ for electron impact excitation of atomic nitrogen from ground state and metastable states: the level numbers of the initial state m and the final state n are defined in Table I. The five rightmost columns give the dimensionless rate parameter values for the electron temperatures listed at the top of each column.

m	n	0.50 eV	1.11 eV	2.45 eV	5.42 eV	12.0 eV
1	2	0.601−1	0.244+0	0.569+0	0.976+0	0.133+1
1	3	0.108+0	0.181+0	0.267+0	0.367+0	0.459+0
1	4	0.273+1	0.283+1	0.232+1	0.239+1	0.322+1
1	5	0.435−1	0.689−1	0.989−1	0.133+0	0.147+0
1	6	0.135−1	0.264−1	0.386−1	0.458−1	0.443−1
1	7	0.110+0	0.166+0	0.229+0	0.315+0	0.385+0
1	8	0.291−1	0.575−1	0.104+0	0.156+0	0.183+0
1	9	0.105+0	0.246+0	0.486+0	0.878+0	0.136+1
1	10	0.320−1	0.663−1	0.999−1	0.132+0	0.147+0
1	11	0.152−1	0.375−1	0.596−1	0.793−1	0.864−1
1	12	0.474+0	0.651+0	0.849+0	0.166+1	0.321+1
1	13	0.274−2	0.421−2	0.613−2	0.865−2	0.986−2
1	14	0.649−2	0.132−1	0.212−1	0.267−1	0.258−1
1	15	0.280−1	0.567−1	0.903−1	0.115+0	0.121+0
1	16	0.472−2	0.125−1	0.265−1	0.414−1	0.446−1
1	17	0.140−1	0.306−1	0.521−1	0.668−1	0.645−1
1	18	0.254−2	0.662−2	0.121−1	0.146−1	0.128−1
1	19	0.134+0	0.300+0	0.714+0	0.181+1	0.364+1
1	20	0.119−1	0.341−1	0.689−1	0.113+0	0.142+0
1	21	0.369−2	0.112−1	0.243−1	0.418−1	0.539−1
2	3	0.542+0	0.172+1	0.306+1	0.364+1	0.400+1
2	4	0.442+0	0.551+0	0.573+0	0.578+0	0.516+0
2	5	0.532+0	0.861+0	0.134+1	0.241+1	0.416+1
2	6	0.185+0	0.199+0	0.171+0	0.173+0	0.204+0
2	7	0.140+0	0.234+0	0.325+0	0.383+0	0.369+0
2	8	0.104+0	0.168+0	0.216+0	0.239+0	0.220+0
2	9	0.325−1	0.601−1	0.744−1	0.902−1	0.105+0
2	10	0.803+0	0.136+1	0.220+1	0.347+1	0.493+1
2	11	0.356−1	0.783−1	0.165+0	0.310+0	0.464+0
2	12	0.630+0	0.899+0	0.918+0	0.895+0	0.915+0
2	13	0.406+0	0.733+0	0.132+1	0.224+1	0.338+1
2	14	0.124−1	0.261−1	0.472−1	0.723−1	0.914−1
2	15	0.636−1	0.113+0	0.164+0	0.190+0	0.167+0
2	16	0.200+0	0.472+0	0.966+0	0.183+1	0.294+1
2	17	0.382−1	0.632−1	0.846−1	0.949−1	0.834−1
2	18	0.624−1	0.144+0	0.285+0	0.516+0	0.793+0
2	19	0.151+0	0.230+0	0.288+0	0.345+0	0.384+0
2	20	0.325+0	0.795+0	0.147+1	0.248+1	0.369+1
2	21	0.319−1	0.977−1	0.170+0	0.225+0	0.257+0
3	4	0.282+0	0.362+0	0.400+0	0.413+0	0.363+0
3	5	0.407+0	0.627+0	0.965+0	0.173+1	0.295+1
3	6	0.160−1	0.303−1	0.411−1	0.446−1	0.432−1
3	7	0.200+0	0.260+0	0.275+0	0.269+0	0.230+0
3	8	0.139+0	0.175+0	0.187+0	0.192+0	0.179+0
3	9	0.828−2	0.127−1	0.164−1	0.243−1	0.340−1
3	10	0.105+0	0.160+0	0.242+0	0.416+0	0.649+0
3	11	0.332+0	0.756+0	0.151+1	0.273+1	0.419+1
3	12	0.472+0	0.653+0	0.628+0	0.563+0	0.542+0
3	13	0.123+0	0.247+0	0.424+0	0.663+0	0.909+0
3	14	0.560−1	0.135+0	0.284+0	0.561+0	0.932+0
3	15	0.280−1	0.537−1	0.833−1	0.994−1	0.883−1
3	16	0.450−1	0.928−1	0.162+0	0.247+0	0.309+0
3	17	0.468−1	0.828−1	0.120+0	0.135+0	0.116+0
3	18	0.167+0	0.409+0	0.867+0	0.170+1	0.279+1
3	19	0.998−1	0.156+0	0.200+0	0.235+0	0.255+0
3	20	0.257−1	0.707−1	0.126+0	0.185+0	0.235+0
3	21	0.157+0	0.388+0	0.751+0	0.133+1	0.204+1

TABLE IV. Calculated effective collision strengths $\gamma_{m\to n}$ for electron impact excitation of singly ionized nitrogen from ground state and metastable states: the level numbers of the initial state m and the final state n are defined in Table II. The five rightmost columns give the dimensionless rate parameter values for the electron temperatures listed at the top of each column.

m	n	1.00 eV	2.52 eV	6.33 eV	15.9 eV	40.0 eV
1	2	0.230+1	0.246+1	0.265+1	0.257+1	0.207+1
1	3	0.264+0	0.289+0	0.324+0	0.320+0	0.256+0
1	4	0.112+1	0.117+1	0.117+1	0.109+1	0.883+0
1	5	0.395+1	0.460+1	0.581+1	0.784+1	0.105+2
1	6	0.308+1	0.375+1	0.499+1	0.706+1	0.995+1
1	7	0.156+1	0.143+1	0.118+1	0.111+1	0.134+1
1	8	0.422+0	0.373+0	0.296+0	0.215+0	0.136+0
1	9	0.119+1	0.105+1	0.891+0	0.720+0	0.523+0
1	10	0.320+0	0.252+0	0.205+0	0.158+0	0.105+0
1	11	0.120+1	0.980+0	0.831+0	0.714+0	0.614+0
1	12	0.173+0	0.158+0	0.141+0	0.117+0	0.837−1
1	13	0.854+0	0.166+1	0.263+1	0.406+1	0.616+1
1	14	0.224+1	0.253+1	0.292+1	0.338+1	0.378+1
1	15	0.333+0	0.345+0	0.346+0	0.306+0	0.221+0
1	16	0.414+0	0.392+0	0.350+0	0.293+0	0.212+0
1	17	0.425−1	0.428−1	0.470−1	0.472−1	0.370−1
1	18	0.583+0	0.550+0	0.511+0	0.425+0	0.328+0
1	19	0.872+0	0.111+1	0.165+1	0.261+1	0.409+1
1	20	0.119+0	0.118+0	0.119+0	0.104+0	0.728−1
1	21	0.320+0	0.426+0	0.633+0	0.980+0	0.150+1
1	22	0.109+0	0.139+0	0.166+0	0.155+0	0.108+0
1	23	0.812−1	0.786−1	0.767−1	0.686−1	0.501−1
2	3	0.604+0	0.569+0	0.607+0	0.661+0	0.710+0
2	5	0.188+1	0.187+1	0.178+1	0.164+1	0.133+1
2	6	0.674+0	0.693+0	0.648+0	0.563+0	0.429+0
2	7	0.853+0	0.780+0	0.605+0	0.420+0	0.253+0
2	8	0.914+0	0.952+0	0.104+1	0.144+1	0.227+1
2	9	0.129+1	0.178+1	0.257+1	0.397+1	0.600+1
2	10	0.468+0	0.358+0	0.268+0	0.212+0	0.188+0
2	11	0.751+0	0.636+0	0.542+0	0.423+0	0.279+0
2	12	0.131+0	0.111+0	0.936−1	0.728−1	0.480−1
2	13	0.218−1	0.259−1	0.317−1	0.344−1	0.288−1
2	14	0.345+0	0.313+0	0.287+0	0.244+0	0.174+0
2	15	0.145+1	0.166+1	0.196+1	0.234+1	0.269+1
2	16	0.510+0	0.649+0	0.908+0	0.141+1	0.216+1
2	17	0.155+0	0.146+0	0.139+0	0.136+0	0.129+0
2	18	0.395+0	0.402+0	0.398+0	0.325+0	0.211+0
2	19	0.178+0	0.194+0	0.210+0	0.186+0	0.126+0
2	20	0.323+0	0.440+0	0.677+0	0.110+1	0.172+1
2	21	0.109+0	0.126+0	0.138+0	0.120+0	0.807−1
2	22	0.374+0	0.496+0	0.748+0	0.121+1	0.196+1
2	23	0.329+0	0.405+0	0.541+0	0.753+0	0.103+1
3	5	0.805−1	0.720−1	0.568−1	0.421−1	0.280−1
3	6	0.439+0	0.434+0	0.428+0	0.400+0	0.328+0
3	7	0.141+0	0.137+0	0.115+0	0.854−1	0.549−1
3	8	0.111+0	0.111+0	0.110+0	0.135+0	0.202+0
3	9	0.840−1	0.595−1	0.401−1	0.284−1	0.220−1
3	10	0.701−1	0.496−1	0.367−1	0.268−1	0.179−1
3	11	0.144+0	0.130+0	0.112+0	0.863−1	0.567−1
3	12	0.622−1	0.533−1	0.478−1	0.392−1	0.267−1
3	14	0.307−1	0.314−1	0.313−1	0.292−1	0.220−1
3	15	0.508−1	0.433−1	0.439−1	0.574−1	0.807−1
3	16	0.175+0	0.193+0	0.248+0	0.356+0	0.498+0
3	17	0.300+0	0.359+0	0.452+0	0.565+0	0.666+0
3	18	0.829−1	0.861−1	0.868−1	0.714−1	0.459−1
3	19	0.252−1	0.273−1	0.294−1	0.257−1	0.171−1
3	20	0.540−1	0.433−1	0.358−1	0.271−1	0.187−1
3	21	0.425−1	0.479−1	0.530−1	0.465−1	0.312−1
3	22	0.280−1	0.298−1	0.327−1	0.379−1	0.455−1
3	23	0.111+0	0.163+0	0.277+0	0.493+0	0.828+0

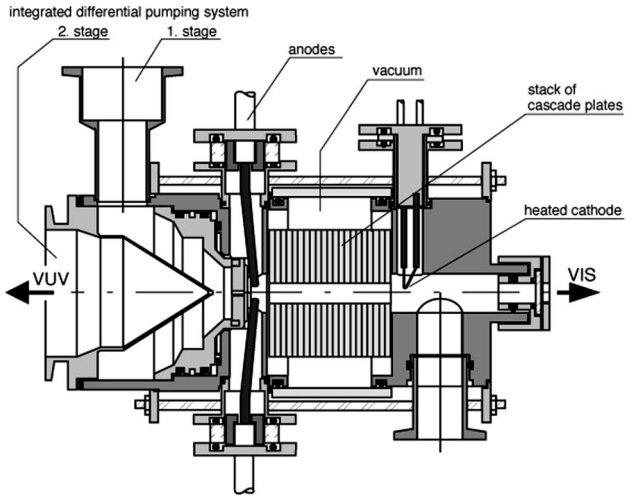

FIG. 7. Discharge chamber.

of platinum. A channeltron electron multiplier, mounted behind the exit slit of the VUV monochromator, was operated in photon counting mode. The counting rate was recorded and stored by means of a computer system together with the respective wavelengths from an incremental encoder.

For the VUV intensity calibration, the low pressure arc was replaced by a 2 mm diameter cascaded arc chamber. This pure He discharge was operated at atmospheric pressure (972 hPA) and 100 A current. It emits continuous radiation down to the helium resonance series limit at 50.4 nm. In order to confirm the continuous intensity calibration in the wavelength region from 53 to 130 nm, a hollow cathode[9] by prescribed design (8 mm in diameter, 60 mm in length) was used, which emits calibrated line radiation. The comparison of these two radiation sources is described shortly in Sec. III B. For more details see Ref. 10.

The low pressure arc as well as the calibration light sources were connected to the VUV system by means of a differential pumping system partly integrated in them. The

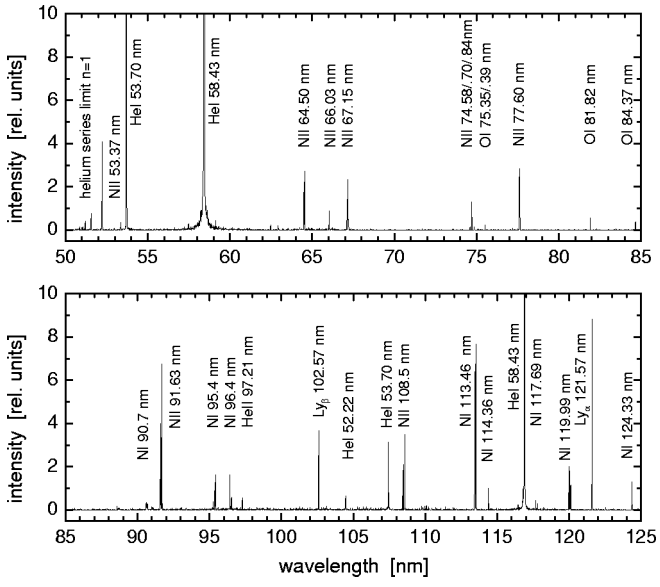

FIG. 8. VUV spectrum of the low-pressure discharge.

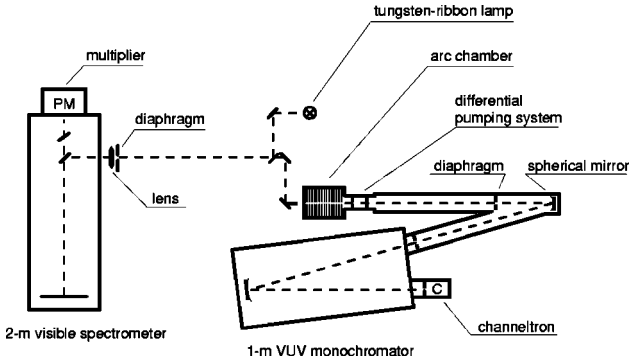

FIG. 9. Experimental setup.

third pumping stage, rigidly connected to the VUV system, reduced the pressure to about 10^{-3} Pa. The first capillary tube of the differential pumping system was positioned only 2 mm from the anodes to keep the cool plasma end layer short.

Both systems observed an area of about 75 μm$\times$350 μm, determined by the entrance slits of each of the two monochromators. The solid angles of the visible and the VUV system were limited to 2×10^{-5} sr defined by diaphragms on both sides. The plasma columns, the central bores of the first pumping stages, and the two diaphragms were aligned along the optical axis of the whole system using a telescope.

B. Calibration of the system response

The calibration of the VUV system response in the spectral range between 53 and 130 nm was based on the continuum radiation of a pure He arc at atmospheric pressure, a method which had been proposed by Thoma.[11] The construction of this calibration device was approximately the same as described above, and the spectra in the visible and VUV spectral range confirm the very low impurity levels (smaller than 0.1 ppm). The continuum radiation of this plasma was recorded with high integration time at 27 selected wavelength points to improve the signal-to-noise ratio. Its spectral radiance can be accurately calculated on the basis of the existing theories, provided that the electron temperature and density are known from diagnostics.

The electron density of the pure He plasma was determined by means of the quadratic Stark broadening of several He I lines. The profiles of five He I lines were investigated, namely of He I 318.8, 396.5, 412.1, 471.3, and 501.6 nm. According to the theoretical broadening calculations of Griem[12] and Kelleher,[13] the electron density was found to be 2.9×10^{16} cm^{-3} with an uncertainty of 6%.

At 100 A and atmospheric pressure, the excited He I states with principal quantum numbers $n\geqslant3$ are above the collision limit and the model of partial thermodynamic equilibrium (PLTE) may be applied for their analysis. This means that the density n_k of a particular excited level k is related to the He II ion ground state density $n_{i,1}$ and the electron density by means of the Saha equation:

$$n_k = n_{i,1} n_e \frac{g_k}{2g_0} \left(\frac{h^2}{2\pi m_e k T_e} \right)^{3/2} \exp\left\{ - \frac{E_k - E_{\text{ion}}}{kT_e} \right\}. \quad (3.1)$$

Herein, g_k and g_0 are the statistical weights of the level k and the He II ground state; E_k and E_{ion} are the pertinent and ionization energies.

The number of He II ground state particles is practically equal to the electron density n_e. Measurements of the absolute He I line emission coefficients therefore yield n_k and subsequently T_e, if n_e is known from the line profiles mentioned above. The present result for T_e is 1.98 eV with a mean uncertainty of 8%. This value and the value listed by Thoma[11] lie close together well within the error bounds. The gas temperature was not measured again, but just taken from Thoma, i.e., $T_g = 13300$ K, because the influence of an error in T_g on the calculated continuum intensity is negligibly small.

Once the plasma parameters are known, the continuum emission coefficient can be calculated as a function of wavelength. In the wavelength range from 510 down to 65 nm, five contributions were taken into account:

(1) the free-bound (f-b) recombination radiation to the levels 2^1S, 2^1P, 2^3S and 2^3P,
(2) the f-b radiation to all levels with principal quantum numbers $n = 3$,
(3) the free-bound radiation to all levels $n \geqslant 3$,
(4) the free-free (f-f) radiation in the electrical field of the ions and
(5) the f-f radiation in the residual electrical field of the He atoms.

All these contributions are explained in more detail in Ref. 10 and in Ref. 14.

The above plasma diagnostics and the continuum calculations were verified by recording the visible He continuum between 420 and 510 nm and using these results for an intensity calibration. The system response derived from the helium continuum and from the tungsten strip lamp agreed within 5% which is consistent with the error limits of n_e alone.

To confirm this continuous intensity calibration of the VUV system at several wavelength points, the normal pressure arc was replaced by a high current hollow cathode which is a reproduction of a well-known transfer standard, calibrated in turn at the Physikalisch Technische Bundesanstalt Berlin. For the purpose of calibration, the operating point was chosen as 1 A/500 V after Hollandt *et al.*[9] For the calibration at the highest and lowest wavelengths, helium and krypton were the filling gases; for the medium wavelength range, argon was used.

Figure 10 shows the response of the VUV system in the range from 53 to 130 nm derived from the helium continuum radiation and the calibrated line radiation of the hollow cathode lamp. The open circles represent the measured values of the helium continuum and are connected by straight lines. The solid symbols represent the system response measured by means of the hollow cathode. It can be seen that the agreement of the calibration methods is very satisfactory in the range from about 65 to 130 nm. In the range below 65 nm, the far red wing of the He I 58.43 nm line of the helium series limit is superimposed on the exponentially decreasing continuum radiation.

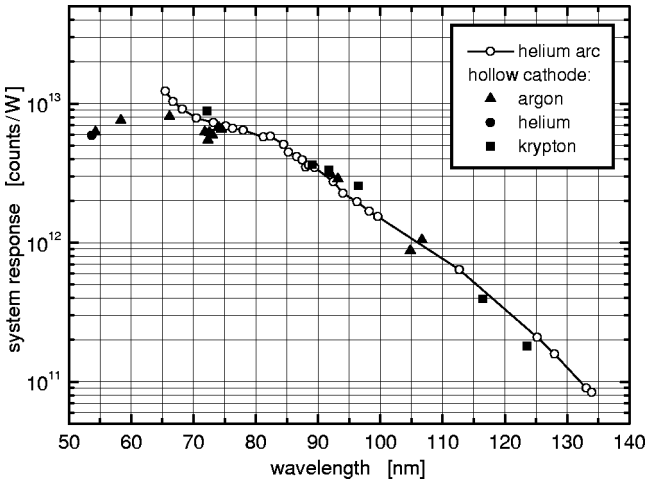

FIG. 10. System response in the VUV spectral range.

The error bounds of the continuous calibration lie between 14% at 130 nm and 33% at 70 nm. The error bound of the calibration by means of the hollow cathode is about 16%. So, the good agreement of both methods gives an uncertainty of the continuous calibration of the system response from 53 to 130 nm which is better than 20%.

IV. PLASMA DIAGNOSTICS

The state of the low-pressure helium plasma is far from local thermal equilibrium. Therefore, Boltzmann and Saha equilibrium relations may not be applied for diagnostic purposes. The nonequilibrium state of the plasma is caused by the low electron density and the energetically high lying excited states of helium. Corresponding to the Maxwellian distribution at electron temperatures from 4.5 to 8.4 eV, only a minor part of the free electrons has energies equal or higher than 20 eV to excite the atoms from the ground state. On the other hand, the radiative lifetimes of the excited states are relatively short compared to the inverse of the electron collision frequency. As a result, a balance between electron-impact excitation and radiative decay establishes itself. This so-called coronal equilibrium is not a property of the whole atomic system but only of the levels lying below the collision limit, which separates these levels from higher lying states. The latter are PLTE distributed according to the electron temperature.

The temperature of the heavy particles is determined by the collisions with free electrons which gain their energy in the electrical field of the discharge. Because of the small mass of the electrons, the kinetic energy transfer to the heavy particles by these collisions is very inefficient resulting in a large difference between the temperatures of the free electrons and the gas.

A. Gas temperature

The knowledge of the gas temperature is of great importance for the calculation of the population densities of the

TABLE V. Parameters and ionization degree of the low-pressure plasma at the various operation points: p designates the discharge pressure, n_e and T_e the density and temperature of the electrons, respectively, n_a the helium atom density, T_g the gas temperature and n_e/n_a the ionization degree for $n_e \ll n_a$.

p(Pa)	n_e(cm^{-3})	T_e(eV)	n_a(cm^{-3})	T_g(K)	n_e/n_a
100	1.83+13	8.4	6.94+15	785	2.64−3
200	2.71+13	7.4	1.36+16	895	2.00−3
400	3.78+13	6.5	2.24+16	1165	1.69−3
800	4.60+13	6.9	3.38+16	1603	1.36−3
1600	5.57+13	5.6	5.50+16	2041	1.01−3
3000	7.00+13	4.5	8.28+16	2579	8.45−4

metastable states of the nitrogen ions. Their densities are mainly determined by diffusion from the near-axis ionization region to the wall of the cylindrically-symmetric discharge chamber. Further on, the knowledge of the gas temperature is important for the diagnostics of the electron density as described in the section below.

Because of the frequently occurring elastic ion-ion collisions, a Maxwellian distribution of the heavy particles is established. This allows the determination of the gas temperature by means of the Doppler broadening of the He I 471.32 nm line. Two components of the triplet transition $4s^3S-2p^3P^o$ are only separated by 1.7 pm. The third component lies 20.3 pm apart and can be resolved spectroscopically in the minus fifth spectral order. The full halfwidth of the pure Doppler profile amounts to at least 5.0 pm convoluted with 2.6 pm from the 2-m monochromator. Because of the low electron density, the Stark broadening can be neglected. In Table V, the gas temperature values which were obtained by a χ^2-fitting procedure[15] are listed.

B. Electron density

The electron density was measured by means of the linear Stark effect in the deuterium Balmer-β line at 485.93 nm. The deuterium concentration was only about 0.01% in order to prevent a considerable proportion of the electrons coming from ionized hydrogen. At the lowest discharge pressure, the full halfwidth of the pure line profile amounts to only 12.7 pm. Deuterium was used in order to minimize the contribution of the Doppler broadening to the measured linewidth.

From the measured line profiles, the electron densities were obtained by applying the aforementioned χ^2-fitting procedure to fit the well-known hydrogen profiles from Vidal, Cooper and Smith,[16] which are nearly independent of the electron temperature. The central dip of each of these calculated profiles is much to deep but does not affect the evaluation. From the difference between the calculated and the measured profile, no systematical error arises by applying the fitting procedure. In Table V the values of the electron densities are listed.

C. Electron temperature

The electron temperature is an important parameter for comparing calculated and measured rate coefficients. For the determination of this parameter, a method first described by Awakowicz and Behringer[17] was used. Therefore, only a brief description will be given in the following.

As a steep function of the plasma pressure, T_e is derived from the He II 468.6 nm emission line, that is the $4\rightarrow 3$ transition in the hydrogen-like He II system. Because of the high excitation energy and the low electron density, it is justified to apply the coronal balance

$$n_e n_{i,1} X_{1,4}(T_e) = n_4 \sum_{k<4} A_{4,k} = n_4 \frac{A_{4,3}}{b_{4,3}}, \tag{4.1}$$

where $n_{i,1}$ denotes the ion ground state number density, $A_{4,3}$ the Einstein coefficient for spontaneous emission and the factor $b_{4,3}$ the branching ratio for level $n=4$. Complete redistribution within the fine structure takes place due to the small energy differences and the high density of the heavy particles. Impurities in this plasma are negligible and the concentrations of hydrogen and nitrogen are very small. Therefore, it may be assumed that the ion number density is very close to the electron density and the overwhelming majority of these ions is in the ground state:

$$n_{i,1} \cong n_i \cong n_e . \tag{4.2}$$

With the measured absolute population density n_4 and the known electron density from Sec. IV B, the actual value of the rate coefficient $X_{1,4}(T_e)$ is given by Eq. (4.1). On the other hand, this rate coefficient can be accurately calculated in the important threshold region by using a semiempirical excitation coefficient after Vriens and Smeets[18] which combines the high-energy Born tail with low-energy near-threshold values obtained from Mansbach and Keck.[19] (See Ref. 17 for further details.) The electron temperatures derived from the comparison of the actual values of the rate coefficient with the calculated ones are listed in Table V.

The higher value of the electron temperature at 800 Pa than that at 400 Pa depends on the variation of the electrical power fed into the discharge which has a local maximum near 900 Pa.

It should be mentioned that the described method is highly accurate even if the cascade contribution to the population of level $n=4$ (about 15%) is not taken into account in Eq. (4.1) because the rate coefficient is extremely steep in the threshold region below 10 eV (see Ref. 17). This steepness would reduce an error of a factor 2 in the measured rate coefficient to one of only 7% in the electron temperature at 5 eV.

V. DETERMINATION OF THE GROUND- AND METASTABLE-STATE DENSITIES AND THE RATE COEFFICIENTS

A. Collisional-radiative model

In order to determine the rate coefficients spectroscopically, it is indispensable to know the population number densities of the respective ground and metastable states. For this purpose, the population densities of the excited states of the two nitrogen systems N I and N II were calculated by applying a collisional-radiative model:

$$n_e\left(\sum_{\sigma=1}^{S} n_\sigma X_{\sigma,m}+\sum_{S<n\neq m}^{N} n_n X_{n,m}\right)+\sum_{n>m} n_n A_{n,m}$$
$$=n_m\left(n_e\left[\sum_{n\neq m} X_{m,n}+S_m\right]+\sum_{n<m} A_{m,n}\right). \quad (5.1)$$

On the left hand side of Eq. (5.1), source terms for the population density of the excited state m are shown. These are the electron-impact excitation from the metastable states σ, including the ground state $\sigma=1$ and from lower lying excited states n. In addition, the electron-impact deexcitation and the cascade processes from all levels higher than m contribute to its population density. Because of the low electron densities in the plasmas investigated here, it can be shown that the three body recombination is negligible. On the right hand side, the depopulation processes are given, namely the electron-impact induced transitions to all other levels n, the impact ionization, and the radiative decay to lower lying levels. As a result, all contributions to the population density of a level m originate directly or indirectly from the ground and metastable states. By contrast, the contribution from the next higher ionization stage has been neglected because its population density is comparatively low due to ambipolar diffusion to the wall.

The above system of equations was evaluated by means of the *ADAS* 208 program. All terms resulting from the collisional calculations of the configurations given in Sec. II were included as well as the important rate coefficients obtained from R-matrix calculations. Energies and transition probabilities were taken from the literature since observed energies and transition probabilities, determined from large structure calculations alone, are likely to be more accurate than those that result from a structure calculation that is constrained by the size of collision problem that it engenders. In the case of N I, the level energies were taken from Wiese *et al.*[20]; for N II those from Eriksson[21] were used. The transition probabilities of N I from Hibbert *et al.*[22] were inserted when available, otherwise they were taken from Wiese *et al.*[20] All transition probabilities of N II were taken from Bell *et al.*[23] The rate coefficients S_m of electron-impact ionization were calculated by the so-called ECIP approximation[24,25] included in *ADAS* 208.

To examine self absorption, the concept of escape factors was applied. This allows a local treatment of reabsorption by reducing the transition probability $A_{m,n}$ to an effective transition probability $\Theta_{m,n}A_{m,n}$. This is due to the fact that a part of the radiative energy emitted elsewhere in the plasma is reabsorbed at another position thus increasing the population density there. A comprehensive review of this subject is given by Irons.[26] In this work, the escape factors of all relevant lines lie between 0.9 and 1.0.

Because of the long radiative life times of metastable states, their population densities are almost entirely limited by diffusion losses to the discharge wall. This process is taken into account by assigning a ''diffusion''-transition probability $A_{\sigma,1}^{\mathrm{diff}}$ $(\sigma=2,3)$ to the metastable states.

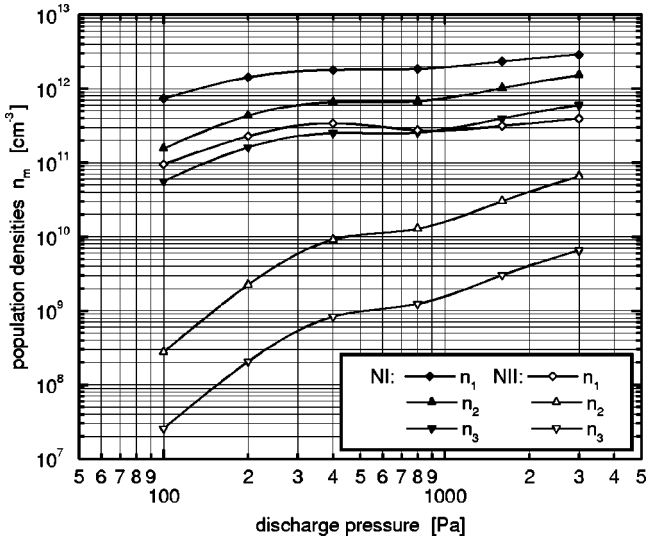

FIG. 11. Population densities of the ground and metastable states of the nitrogen atom (N I) and ion (N II).

B. Diffusion

The solution of the time-dependent diffusion equation for a cylinder symmetrical geometry is given by

$$n(r,t)=n(0)J_0\left(\frac{2.405r}{R}\right)\exp\{-t/\tau_{\mathrm{diff}}\}, \quad (5.2)$$

with the Bessel function J_0, the cylinder-radius R, the on-axis particle density $n(0)$ at time $t=0$, and the time constant for radial diffusion τ_{diff}. $A_{\sigma,1}^{\mathrm{diff}}$ is defined as the inverse of τ_{diff}, which can be calculated from the characteristic diffusion length Λ_{diff}:

$$A_{\sigma,1}^{\mathrm{diff}}=\frac{1}{\tau_{\mathrm{diff}}}=\frac{D}{\Lambda_{\mathrm{diff}}^2}=D\left(\frac{2.405}{R}\right)^2. \quad (5.3)$$

For further details, see McDaniel and Mason.[27] To evaluate the diffusion coefficient D for the N-He system, a potential function after Chapman and Cowling[28] was taken:

$$\Phi(r)=\frac{d}{r^\delta}, \quad (5.4)$$

with the potential parameters $d=13.73$ eV Å$^{6.23}$ and $\delta=6.23$ after Amdur *et al.*[29] The calculation of the diffusion coefficient for the N^+-He system was based on a 12-6-4 potential

$$\Phi(r)=\frac{\epsilon}{2}\left[(1+\gamma)\left(\frac{r_m}{r}\right)^{12}-4\gamma\left(\frac{r_m}{r}\right)^{6}-3(1-\gamma)\left(\frac{r_m}{r}\right)^{4}\right] \quad (5.5)$$

after Mason and Schamp.[30] Herein $\gamma=0.125$, $\epsilon=0.0439$ eV and $r_m=2.29$ Å denote potential parameters also taken from Ref. 30. The binary diffusion coefficient was calculated after Kihara (see Ref. 31) and yielded the ambipolar diffusion coefficient from the measured temperatures as

$$D_a\cong D\left(1+\frac{T_e}{T_g}\right). \quad (5.6)$$

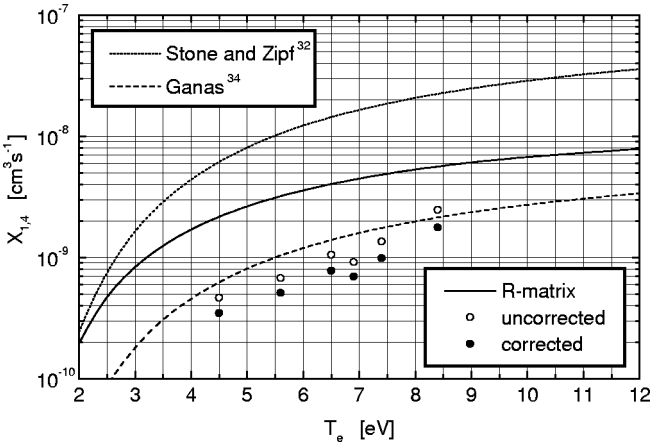

FIG. 12. N I-rate coefficient $X_{1,4}$ for electron impact excitation of level $(^3P)3s\ ^4P$ from the ground state $2p^3\ ^4S^o$.

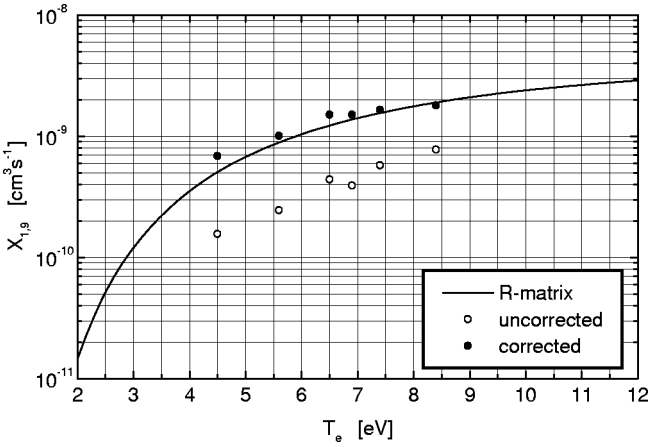

FIG. 14. N I-rate coefficient $X_{1,9}$ for electron impact excitation of level $(^3P)3p\ ^4S^o$ from the ground state $2p^3\ ^4S^o$.

The resulting $A_{\sigma,1}^{\mathrm{diff}}$ values range from 6.2×10^4 to 2.8×10^5 s^{-1} for the metastable states of the nitrogen atom and from 1.8×10^6 to 5.1×10^7 s^{-1} for the metastables of the ion. Since both diffusion coefficients decrease with increasing pressures, diffusion is reduced but in no case negligible for the metastable levels.

C. Ground- and metastable-state population densities and rate coefficients

Dividing the collisional-radiative model [Eq. (5.1)] by the ground-state population n_1 yields relative population densities $\eta_m = n_m/n_1$ for every level m of the system. The ground-state density may now be obtained by inserting the measured absolute level populations n_m into

$$n_1 = \frac{n_m}{\eta_m}. \tag{5.7}$$

However, this means that the accuracy of the resulting ground-state values depends on those calculated rate coefficients which are decisive for the bulk of the level populations n_m. Because highest accuracy of the collisional calculation is expected for dipole transitions, only those levels m which obtain the main part of their population via ''dipole allowed'' electron excitation processes have been used to determine the ground-state population. In addition, the oscillator strengths yielded by *AUTOSTRUCTURE* provide a fairly good criterion for the modeling of the respective nitrogen target which the following collisional-radiative calculations were based on. Finally, mean values for the ground-state populations have been calculated from four single N I and 9 single N II ground-state values, respectively.

The resulting values for the ground- and metastable-state densities are shown in Fig. 11 where the steep decrease of the N II metastables is due to the ambipolar diffusion.

On the basis of these values we determined the rate coefficients by applying the already described collisional-radiative model, written as

$$X_{1,m}K_m = \frac{n_m}{n_e n_1}\sum_{n<m}\Theta_{m,n}A_{m,n}. \tag{5.8}$$

Herein the factor K_m represents the influence of electron-impact excitation from the metastable states, the spontaneous decay from higher excited states (cascade processes) and electron-impact ionization on the population of the level m.

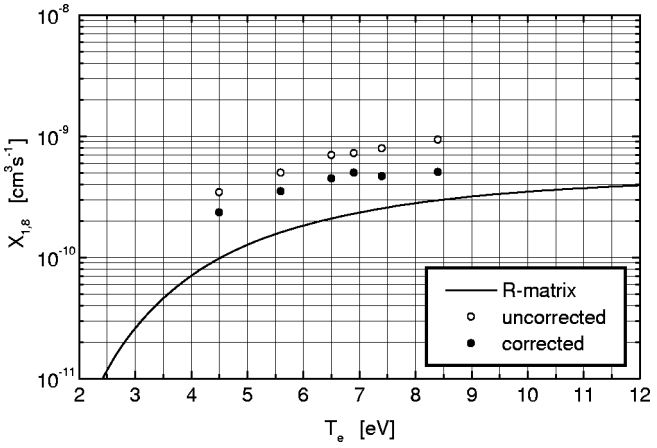

FIG. 13. N I-rate coefficient $X_{1,8}$ for electron impact excitation of level $(^3P)3p\ ^4P^o$ from the ground state $2p^3\ ^4S^o$.

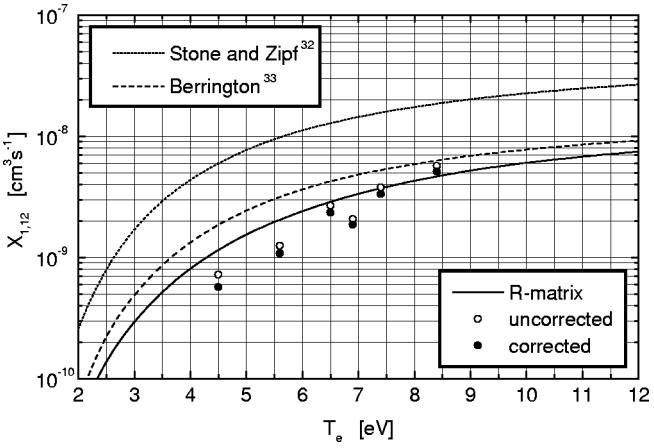

FIG. 15. N I-rate coefficient $X_{1,12}$ for electron impact excitation of level $2p^4\ ^4P$ from the ground state $2p^3\ ^4S^o$.

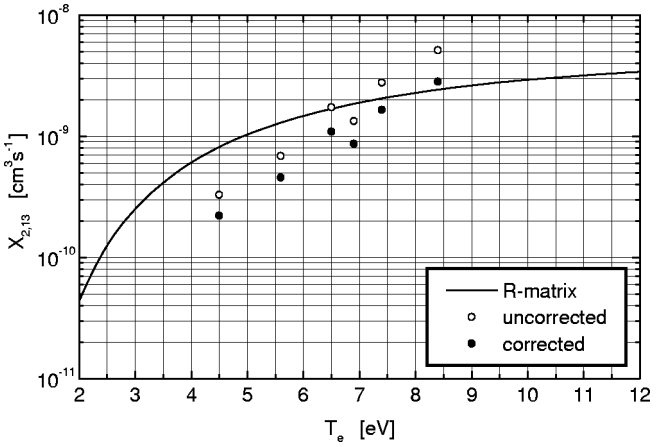

FIG. 16. N I-rate coefficient $X_{2,13}$ for electron impact excitation of level $(^1D)3s'\ ^2D$ from the metastable state $2p^3\ ^2D^o$.

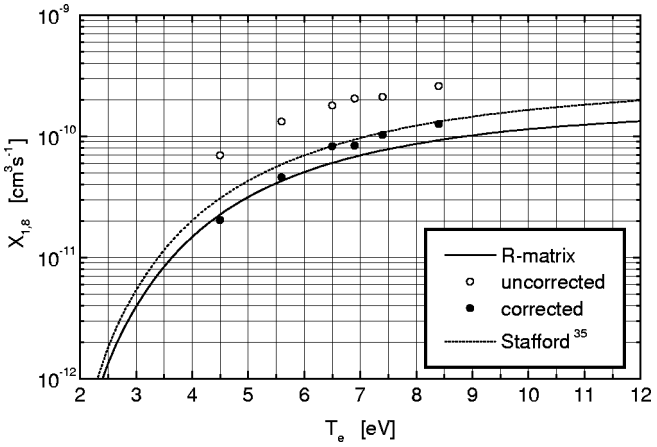

FIG. 18. N II-rate coefficient $X_{1,8}$ for electron impact excitation of level $(^2P)3s\ ^1P^o$ from the ground state $2p^2\ ^3P$.

All of the transitions which were used for the experimental determination of level population densities n_m, via absolute line emission coefficients $\varepsilon_{Lm,n}$, given by

$$n_m = \varepsilon_{Lm,n} \frac{4\pi}{h\nu_{m,n} A_{m,n}}, \tag{5.9}$$

are shown in Figs. 3 and 4 for the neutral atom and in Figs. 5 and 6 for the the singly ionized ion. Some of these spectral lines can also be seen in the VUV spectrum plotted in Fig. 8. The optical depths of all relevant emission lines were calculated and they were found to be completely negligible.

The measured rate coefficients determined as described in Eq. (5.8) are shown by solid circles in Figs. 12–23 along with the R-matrix calculations. The open circles, designated by ''uncorrected,'' represent rate coefficients $X_{\sigma,m}$ which one would get from Eq. (5.8) without taking into account the factor K_m. So, the difference between the ''corrected'' and ''uncorrected'' values shows the influence of all other processes than collisional excitation from the ground state to the population of level m.

Corresponding data from the literature is also included in the diagrams: for the neutral atom, measured cross sections from beam foil experiments carried out by Stone and Zipf[32] for the transitions $2p^3\ ^4S^o - 2p^2 3s\ ^4P$ (Fig. 12) and $2p^3\ ^4S^o - 2p^4\ ^4P$ (Fig. 15), an earlier R-matrix calculation performed by Berrington *et al.*[33] for the transition $2p^3\ ^4S^o - 2p^4\ ^4P$ (Fig. 15) and a Born approximation from Ganas[34] for the transition $2p^3\ ^4S^o - 2p^2 3s\ ^4P$ (Fig. 12). For singly ionized nitrogen, a R-matrix calculation has been performed recently by Stafford *et al.*[35] Figures 18–23, which show the N II rate coefficients, do also include data from this work, as far as available.

VI. DISCUSSION AND CONCLUSIONS

The comparison of experimental and theoretical Maxwell averaged rate coefficients, a small selection is shown in Figs. 12–23, shows a broad trend of agreement. There are, however, a number of cases where the divergence is more substantial. For example, for the transitions $2p^2\ ^3P - 2p3d^3P^o$ (Fig. 23) and $2p^2\ ^3P - 2p3d^3D^o$ (Fig. 22) in N II, experiment is about a factor 10 less than theory. There is in fact some systematic trend between experiment/theory ratios for excitation to the $n=2$ shell and to the $n=3$ shell with the latter relatively lower. Studies in recent years on convergent close-coupling (CCC) methods in the intermedi-

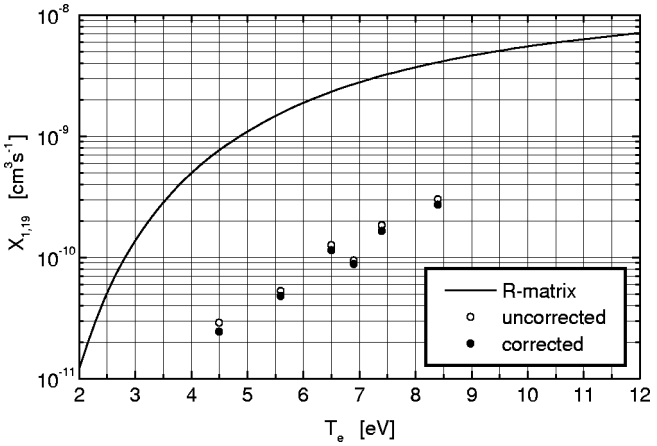

FIG. 17. N I-rate coefficient $X_{1,19}$ for electron impact excitation of level $(^3P)3d\ ^4P$ from the ground state $2p^3\ ^4S^o$.

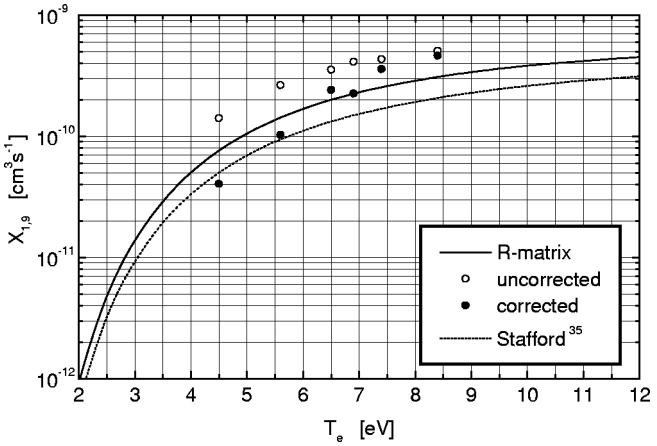

FIG. 19. N II-rate coefficient $X_{1,9}$ for electron impact excitation of level $2p^3\ ^1D^o$ from the ground state $2p^2\ ^3P$.

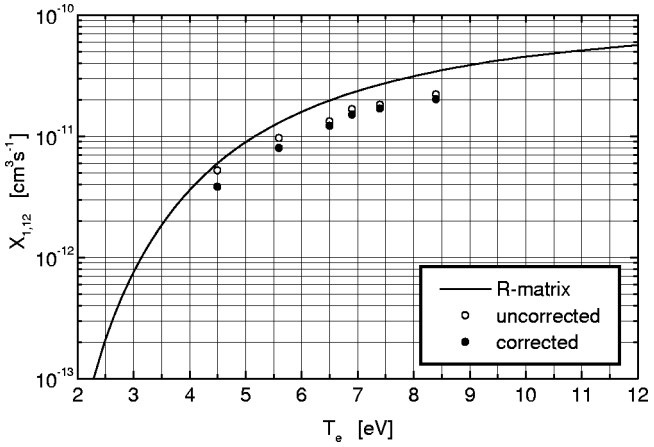

FIG. 20. N II-rate coefficient $X_{1,12}$ for electron impact excitation of level $(^2P)3p\ ^3S$ from the ground state $2p^2\ ^3P$.

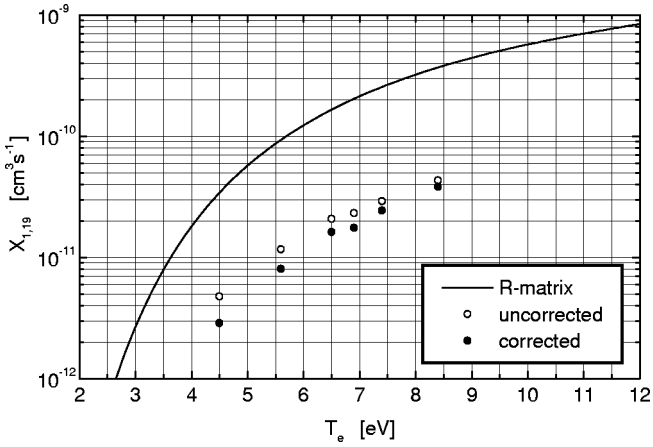

FIG. 22. N II-rate coefficient $X_{1,19}$ for electron impact excitation of level $(^2P)3d\ ^3D^o$ from the ground state $2p^2\ ^3P$.

ate energy regime for neutral and near neutral atoms have indicated a problem arising from a deficient treatment of allowing for ''loss of flux to the continuum'' in the type of R-matrix calculations used here. The new CCC method[36] and large pseudo-state R-matrix treatments[37] solve this problem for simple systems (H, He and iso-electronic ions, neutral Be and B) but have not been applied yet to more complex systems such as N I and N II. The continuum influence is larger for the $n=3$ excitations, less pronounced for strong dipole transitions and decreases with increasing ion charge. lt is suggested that for the $3d$ excitations from the ground in N II, the effect is likely to be a decrease in the theoretical cross section of 25% at most.

The internal correctness of the present R-matrix calculations is indicated by the good agreement with Stafford *et al.*[35] although the target structures will be somewhat different. Stafford *et al.* did not however include the $2p-3d$ excitations. Provided very high partial wave contributions are included in the cross-sections and the target oscillator strengths for the transitions are correct, large errors are unlikely. The comparison with Born cross sections (even though with again a slightly different target structure) confirms this. Thus it would be surprising to find the theoretical $2p^2\ ^3P-2p3d^3P^o$ and $2p^2\ ^3P-2p3d^3D^o$ rate coefficients in N II to be wrong by more than a factor 2.

Some observations have been made of VUV lines of N II in detached radiating divertor studies at the Joint European Torus (JET). In these experiments, N_2 is puffed into the divertor region which initiates a transition to a strongly radiating plasma detached from the divertor strike zones. Such a plasma has an electron temperature $T_e<\sim 5$ eV and an electron density n_e in the range 5×10^{13} to 10^{14} cm^{-3}. The uncertainty in the intensity calibration of the JET VUV spectrometer is believed to be less than a factor 2. We have JET measurements of four lines on the triplet side, namely, $2p^2\ ^3P-2s2p^3\ ^3S^o$ (64.50 nm), $2p^2\ ^3P-2p^3\ ^3D^o$ (108.50 nm), $2p^2\ ^3P-2p^3\ ^3P^o$ (91.63 nm), and $2p^2\ ^3P-2p3d^3P^o+^3D^o$ (52.97/53.37 nm). The latter is an unresolved blend in the JET spectrometer. The observed spectral line ratios time histories in JET show an oscillatory behavior as the divertor strike zone is actively scanned across the target plates, however this variation is $<25\%$ and so we expect the error bound on the JET observed ratios to be $\sim 50\%$. For the comparison, we conducted two excited population calculations. The first used the theoretical R-matrix collision data

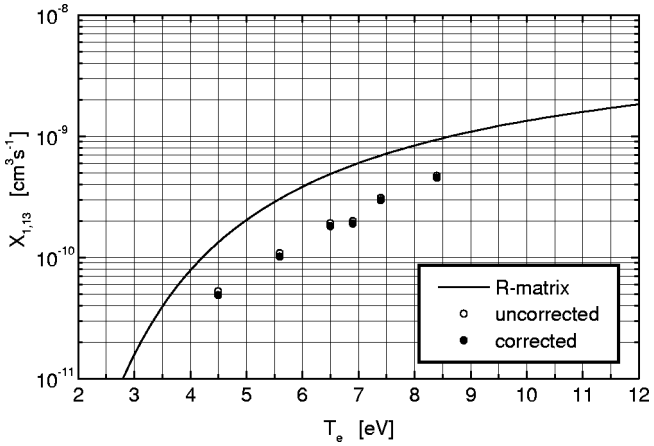

FIG. 21. N II-rate coefficient $X_{1,13}$ for electron impact excitation of level $2p^3\ ^3S^o$ from the ground state $2p^2\ ^3P$.

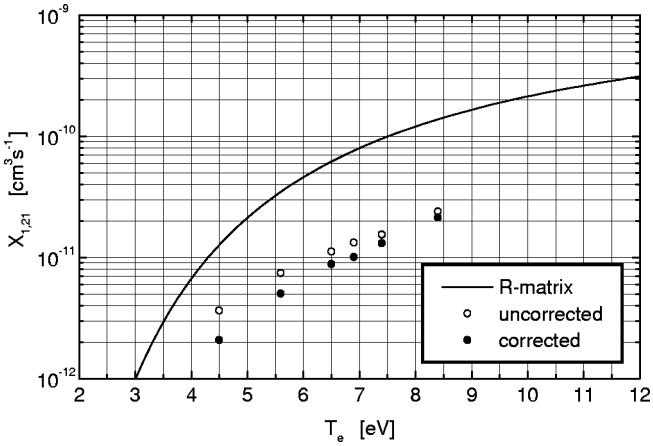

FIG. 23. N II-rate coefficient $X_{1,21}$ for electron impact excitation of level $(^2P)3d\ ^3P^o$ from the ground state $2p^2\ ^3P$.

calculated as part of this work. For the second, each theoretical rate coefficient on the triplet side originating from the $2p^2\ ^3P$ ground state has been scaled by the difference between the experimental rate coefficient and the theoretical rate coefficient at 6 eV. The population calculations forced the singlet metastables to be in quasi-static balance with the ground state. The metastable populations have only a small influence on the four triplet lines considered here. We used the *ADAS* code *ADAS* 207 to prepare contour plots of the line emissivity ratios (1) 645/1085 nm, (2) 645/916 nm and (3) 645/533 nm on the temperature versus density plane. Ratios (1) and (2) are temperature dependent only. Ratio (3) is sensitive to both temperature and density. It is found that the JET observed ratios (including error bars) overlap the JET plasma conditions for ratios (1) and (3) and just miss for ratio (2) in the case of the first (theoretical cross-section) population calculation. The contour maps indicate a JET plasma at $T_e \sim 4$ eV and $n_e \sim 7\times10^{13}\ cm^{-3}$. For the second (experimentally adjusted cross section) case, the JET ratios miss severely for both plots (1) and (2) but overlap plot (3). Thus the JET data does not appear to support the laboratory deduced rates for these triplet lines.

It is to be noted that ratios (1) and (2) above are markedly temperature sensitive due to the difference in excitation energies from the ground to the upper level of the transitions. In a plasma with temperature gradients such as that of the JET divertor, some separation of the emitting layers for the low and high excitation energy lines is to be expected. Thus the ''miss'' for ratio (2) for the JET data in comparison with the theoretical cross section data errs in the expected direction. On this basis, we might be led to query the apparent temperatures in the experimental deductions of the present paper. It is difficult to separate a temperature layering effect from non-Maxwellian effects. Equally, new studies of JET divertor conditions suggest that there may be substantial deviations from Maxwellian electron distributions there also. The JET data used in the previous paragraphs was for a fairly dense plasma which, it was hoped, minimized the possibility of non-Maxwellian effects. Non-Maxwellian effects might be expected to show most strongly on the higher excitation energy strong dipole rate coefficients which is the effect seen here.

The placing of the present experimental rates against the theoretical ones has used a normalization factor derived from an unbiased equal weighting of a number of the rates. An alternative policy is to group the transitions into those involving low excitation energies (mostly $\Delta n = 0$ transitions) and those involving higher transition energies (mostly $\Delta n = 1$ transitions). This would help in probing anomalies of the electron distribution function.

In summary, an extended comparison has been made of experimentally measured rate coefficients with theoretical rates also calculated as part of this article. A broad agreement is achieved between theory and experiment within $\sim$ factor 2. However, there are two or three transitions, involving excitation to the $n=3$ shell which are more severely discrepant. Although there are some grounds for increasing the expected errors in the theoretical results, these are insufficient to explain the discrepancies. Additional evidence from JET measurements points to electron temperature as the primary factor. Although deviations from Maxwellian distributions can occur in low density plasmas, a clear signature is not yet available for the present experiment or the divertor fusion plasma. The ability presented by the present experiment to contrast behavior with divertor plasma is of considerable value for probing these issues and the investigation is continuing.

ACKNOWLEDGMENTS

The authors wish to thank the Dr. Johannes Heidenhain Stiftung for the extensive financial support of this work.

APPENDIX NOTE

The complete data yielded by this work, i.e., all calculated collision strengths and Maxwellian-averaged rate parameters as well as diagrams of all measured rate coefficients are available from the authors on request. Furthermore, the *ADAS* data base contains the rate parameters as adf04 files, named *nlike_rf97#n0.dat* and *clike_rf97#n1.dat*.

[1] H. P. Summers and L. Wood, ''Ionization, Recombination and Radiation of Impurities in Plasmas. An Interactive Atomic Data and Applications Structure,'' JET-R(88)06 (1988).
[2] N. R. Badnell, J. Phys. B **19**, 3827 (1986).
[3] W. Eissner, M. Jones, and H. Nussbaumer, Comput. Phys. Commun. **8**, 270 (1974).
[4] K. A. Berrington, W. B. Eissner, and P. H. Norrington, Comput. Phys. Commun. **92**, 290 (1995).
[5] V. M. Burke, P. G. Burke, and N. S. Scott, Comput. Phys. Commun. **69**, 76 (1992).
[6] V. M. Burke and C. J. Noble, Comput. Phys. Commun. **85**, 471 (1995).
[7] K. A. Berrington, P. G. Burke, K. Butler, M. J. Seaton, P. J. Storey, K. T. Taylor, and Y. Yan, J. Phys. B **20**, 6379 (1987).
[8] H. Maecker and S. Steinberger, Z. Angew. Phys. **33**, 456 (1967).
[9] J. Hollandt, M. Kühne, and B. Wende, Appl. Opt. **33**, 68 (1994).
[10] R. M. Frost and P. Awakowicz, Appl. Opt. **36**, 9 (1997).
[11] P. Thoma, Z. Naturforsch. A **35a**, 808 (1980).
[12] H. R. Griem, *Spectral Line Broadening by Plasmas* (Academic, New York, 1974).
[13] D. Kelleher, thesis, University of Maryland, 1977, Technical Note BN-865.
[14] P. Thoma, thesis, Lehrstuhl für Techn. Elektrophysik, Techn. Univ. München, 1978.
[15] K. Jeß, V. Helbig, F. Greiner, J. Kaspasreit, V. Rohde, and T. Weirauch, J. Quant. Spectrosc. Radiat. Transf. **41**, 69 (1989).
[16] C. R. Vidal, J. Cooper, and E. W. Smith, Astrophys. J. Suppl. **214**, 37 (1973).
[17] P. Awakowicz and K. Behringer, Plasma Phys. Controlled Fusion **37**, 551 (1995).
[18] L. Vriens and A. H. M. Smeets, Phys. Rev. A **22**, 940 (1980).
[19] P. Mansbach and J. Keck, Phys. Rev. **181**, 275 (1969).
[20] W. L. Wiese, J. R. Fuhr, and T. N. Deters, *Transition Probabilities of Carbon, Nitrogen and Oxygen: A Critical Data Compilation*, J. Phys. Chem. Ref. Data, Monograph No. 7 (1996).
[21] K. B. S. Eriksson, Phys. Scr. **28**, 593 (1983).
[22] A. Hibbert, E. Biemont, M. Godefroid, and N. Vaeck, Astron. Astrophys., Suppl. Ser. **88**, 505 (1991).
[23] K. L. Bell, A. Hibbert, and R. P. Stafford, Phys. Scr. **52**, 240 (1995).
[24] A. Burgess, *Proceedings Symposium on Atomic Collision Processes in Plasmas* (Culham, Ukaea, 1964).
[25] A. Burgess, H. P. Summers, D. M. Cochrane, and R. W. P. McWhirter, Mon. Not. R. Astron. Soc. **179**, 275 (1977).
[26] F. E. Irons, J. Quant. Spectrosc. Radiat. Transf. **22**, 1 (1979).
[27] E. W. McDaniel and E. A. Mason, *The Mobility and Diffusion of Ions in Gases* (Wiley, New York, 1973).

[28] S. Chapman and T. G. Cowling, *The Mathematical Theory of Non-Uniform Gases* (Cambridge University Press, Cambridge, 1970).
[29] I. Amdur, E. A. Mason, and J. E. Jordan, J. Chem. Phys. **27**, 527 (1957).
[30] E. A. Mason and H. W. Schamp, Jr., Ann. Phys. (N.Y.) **4**, 233 (1958).
[31] E. A. Mason, J. Chem. Phys. **27**, 75 and 782 (1957).
[32] E. J. Stone and E. C. Zipf, J. Chem. Phys. **58**, 4278 (1973).
[33] K. A. Berrington, P. G. Burke, and W. D. Robb, J. Phys. B **8**, 2500 (1975).
[34] P. S. Ganas, J. Chem. Phys. **59**, 5411 (1973).
[35] R. P. Stafford, K. L. Bell, A. Hibbert, and W. P. Wijesundera, Mon. Not. R. Astron. Soc. **268**, 816 (1994).
[36] I. Bray and A. Stelbovics, Adv. At., Mol., Opt. Phys. **35**, 209 (1995).
[37] K. Bartschat, E. T. Hudson, M. P. Scott, P. G. Burke, and V. M. Burke, J. Phys. B **29**, 115 (1996).
[38] C. E. Moore, *Atomic Energy Levels*, U.S. National Bureau of Standards, Circular 467, Washington (1949).